

## Research Article

# Numerical and Analytical Study of Bladder-Collapse Flow

**M. Tziannaros and F. T. Smith**

*Department of Mathematics, UCL, Gower Street, London WC1E6BT, UK*

Correspondence should be addressed to M. Tziannaros, [mtziannaros@gmail.com](mailto:mtziannaros@gmail.com)

Received 22 October 2011; Accepted 23 November 2011

Academic Editor: Ebrahim Momoniat

Copyright © 2012 M. Tziannaros and F. T. Smith. This is an open access article distributed under the Creative Commons Attribution License, which permits unrestricted use, distribution, and reproduction in any medium, provided the original work is properly cited.

Understanding and quantifying more of the workings of the human bladder motivates the present industry-supported study. The bladder performance in terms of the urinary velocities produced tends to be dominated by the internal fluid dynamics involved, in the sense that the bladder wall moves in a body-prescribed way. The enclosed urine flow responds to this wall movement, and there is relatively little feedback on the wall movement. Combined computational work and special-configuration analysis are applied over a range of configurations including computational and analytical results for the circle and sphere as basic cases; models of more realistic bladder shapes; the end stage of the micturition process where the bladder is relatively squashed down near the urethral sphincter and localised peak speeds arise. The combination of approaches above can be extended to allow for interaction between wall shape and flow properties such as internal pressure if necessary.

## 1. Introduction

The investigation here involves industrial motivation and support with a biomedical setting which is strongly affected by fluid dynamics and is treated by computations along with analysis including matched asymptotic expansions. Industry with a view to incontinence devices in particular wishes to know of the induced velocities and pressures in a bladder, wishes for more mathematical approaches, and wishes eventually to understand more of realistic three-dimensional dynamics.

The workings of the human lower urinary tract—of which a diagram is shown in Figure 1—are clearly of much interest. Relevant background material and some studies are in [1–6]. Yet scant attention has been paid to increased understanding and quantitative prediction for the bladder particularly. The bladder wall tends to move in a body-prescribed way, the enclosed urine flow responds to this wall movement, and there is comparatively little feedback from the flow behaviour on the wall movement. Computational results are obtained below by use of a relatively simple approach [7] which has the benefits of wide

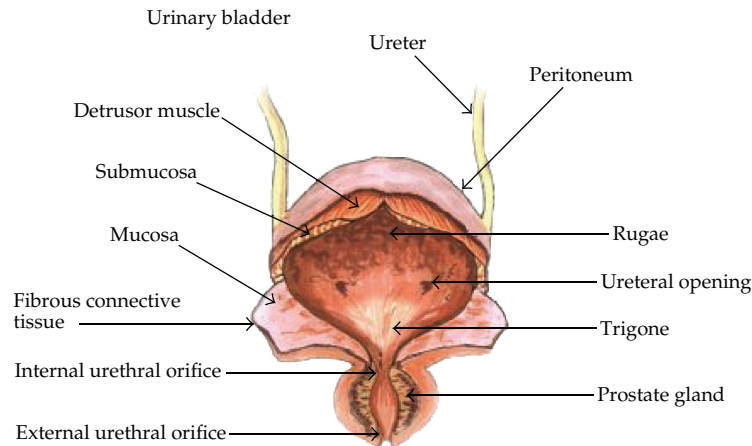


**Figure 1:** Diagram taken from [8] of sections through the urinary tract and more specifically the ureters, parts of the bladder and the urethra.

application allied with accuracy. Special-configuration analysis also proves a valuable and insightful approach applying over a wide range of configurations.

Around 15% of women and 7% of men suffer from incontinence, while benign prostatic hyperplasia occurs in more than 80% of men aged 75 [1]. A recent statistic published by Astellas Pharma shows that, in the UK alone 5 million people have bladder problems. At the same time, 1 in 5 people over the age of 40 have a urinary problem. Therefore, diagnosing and curing problems of the lower urinary tract are vital. This is the aim of urodynamics. Indeed in urodynamics examination measurements such as the pressure level in various regions of the lower urinary tract, volume of urine and flow rate are taken and then used to indicate underlying pathologies. It is important to understand the physical properties of the tract and its contained flow of urine as several pathologies can exhibit similar symptoms. Developing a mathematical tool is potentially important in this regard as it could be used to check or validate current tests and measurements. It can also indicate further predictive tests that may prove useful in diagnosis by providing more understanding of the mechanics of the lower urinary tract. The complexity of a system such as the bladder means that a lot of important properties could be taken into account and hence investigated.

An excellent description of urodynamics is given by [5] and others. Urodynamics is a group of diagnostic procedures (as hinted at the beginning of this section) that are performed to evaluate disorders related to the bladder and the urethra. The parameters which are measured during a urodynamic procedure mainly include pressure and flow rate. Thus far, procedures have been relatively insufficient in suggesting treatments for the problems involved. Developments in treatments depend to a large extent on understanding the behaviour of the system. The present research aims at addressing part of that behaviour by tackling the mechanical aspects of the bladder and its contained fluid. The high distensibility and complex anatomy of the system in parallel with the large disturbances in shape make this task challenging and tend to put it outside the range of previous modeling. The study is directed at tackling shapes like the ones shown in the cystourethrograms in Figure 2.

The methodology is described in Section 2, this being based on numerical work combined with special-case and end-stage analysis. The results then follow in Section 3, after which Section 4 presents final comments.

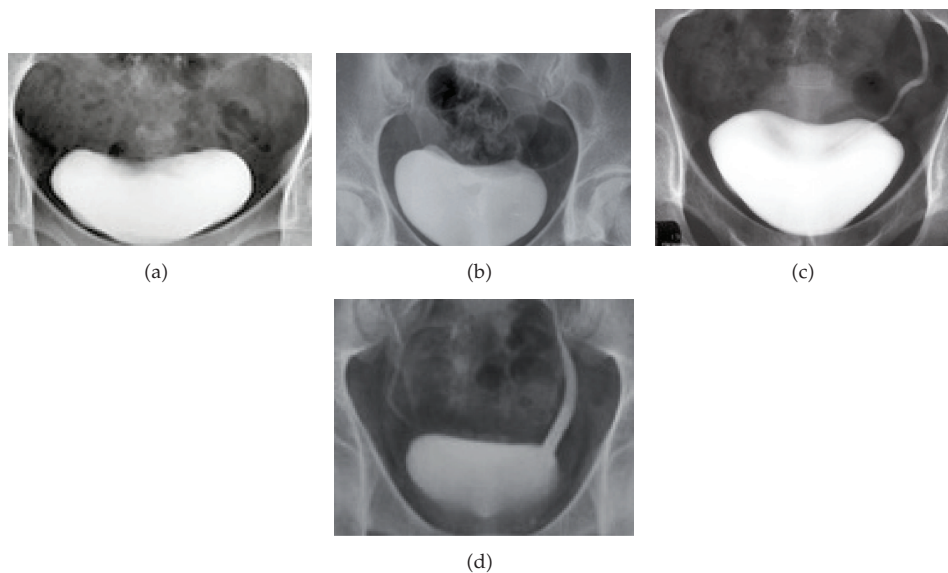


**Figure 2:** Shapes of different bladders later on during micturition, taken by a Voiding Cystourethrogram (a) [2], (b) [3], (c) [2], (d) [9]. The light patch in the middle is the bladder. Also visible are the bones, and, in some instances such as (c) and (d), we can see the right ureter.

## 2. Methods

Part of the theoretical background hinges on the detailed relationship between the full Navier-Stokes equations

$$\begin{aligned}\frac{\partial \mathbf{u}}{\partial t} + \mathbf{u} \cdot \nabla \mathbf{u} &= -\frac{\nabla p}{\rho} + \nu \nabla^2 \mathbf{u}, \\ \nabla \cdot \mathbf{u} &= 0,\end{aligned}\tag{2.1}$$

and the interactive boundary-layer system with unknown pressure,

$$\frac{\partial u}{\partial t} + u \frac{\partial u}{\partial x} + v \frac{\partial u}{\partial y} = -\frac{1}{\rho} \frac{\partial p}{\partial x} + \nu \frac{\partial^2 u}{\partial y^2},\tag{2.2}$$

$$\frac{\partial u}{\partial x} + \frac{\partial v}{\partial y} = 0,\tag{2.3}$$

explored by papers [7, 10–14]. These in many cases show the important role of jump conditions based on the inviscid Euler system

$$\frac{\partial \mathbf{u}}{\partial t} + \mathbf{u} \cdot \nabla \mathbf{u} = -\frac{\nabla p}{\rho},\tag{2.4}$$

$$\nabla \cdot \mathbf{u} = 0,\tag{2.5}$$

to smooth out discontinuities in (1) in industrial and biomedical problems. In the present study, the governing equation of concern is Laplace's equation for the stream function  $\Psi$ ,

$$\nabla^2\Psi = 0, \quad (2.6)$$

many extra features arise from the complicated boundary shapes involved. The Reynolds numbers for the collapsing bladder flow have quite large values in general and as a consequence the flow is effectively unsteady, incompressible, and inviscid. It is also irrotational because it starts from rest. Hence, there is an unknown velocity potential and corresponding stream function to be found, satisfying (2.6). Urine flow velocity components  $u = \partial\Psi/\partial y$ ,  $v = -\partial\Psi/\partial x$  are used in terms of Cartesian coordinates  $x$ ,  $y$  in the two-dimensional setting, and time is denoted by  $t$ ; in axisymmetric configurations, a similar stream-function equation holds. There are three main aspects 1–3 to the methods employed.

### 2.1. Numerical Method

The numerical scheme used is an iterative finite difference method with boundary interpolation. This well-established method is efficient around the boundaries of the model shapes of interest (which are highly distorted in general), and it also deals readily with topological changes [7, 15], suggesting application allied with accuracy and flexibility. A standard five-point form is used at almost all internal points supplemented by an in-out criterion based on extending the idea of [7] to refine boundary interpolation. The boundary interpolation with the iterative finite differencing handles the present complex situations in terms of the boundary condition on the tangential derivative of the stream function,  $\partial\Psi/\partial s$ , where  $\partial s = \sqrt{(\partial x^2 + \partial y^2)}$  is the distance element along the boundary. The condition now only depends on the shape function  $F(x, y, t)$ , which can in particular describe complex shapes.

The form of the input boundary condition for shapes  $F = y - f(x, t) = 0$  is, from the kinematic condition,

$$\frac{\partial\Psi}{\partial s} = -\frac{F_t}{(F_y^2 + F_x^2)^{1/2}}. \quad (2.7)$$

The modelled shapes that the vessel takes during micturition in the case of human bladder evacuation are specified as follows and presented in Figure 3. The vessel collapses in time using the three-dimensional steady flow equation from [7] but in two spatial dimensions and time: time here replaces the third spatial dimension of [7]. With the necessary alterations, the function for the present collapse becomes

$$F_u(x, y, t) = y - (1 - x^2)^{1/2} + \sum_{m=1}^n h_m t^2 e^{-8(x-k_m)^2}, \quad (2.8)$$

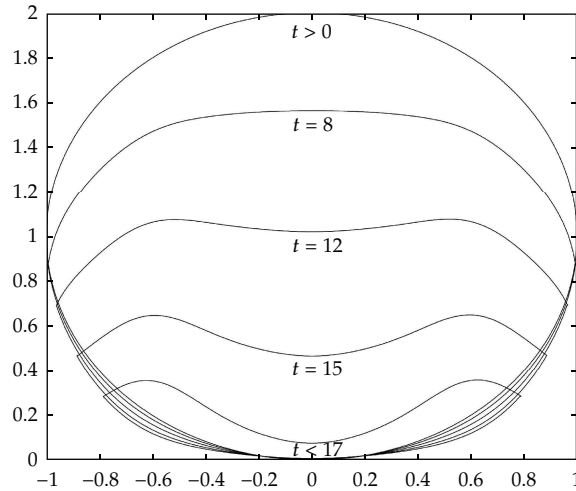


**Figure 3:** Shapes that the vessel takes at different times as it collapses with a cardioidal-like shape, in the model.

where  $h_m$  is the collapsing factor at the  $x = k_m$  position of the vessel, of the  $m$  out of  $n$  movements. This represents the upper half of the function, and we similarly have a lower one given as

$$F_l(x, y, t) = y + (1 - x^2)^{1/2} - \sum_{p=1}^q h_p t^2 e^{-8(x-k_p)^2}, \tag{2.9}$$

where  $h_p$  is the collapsing factor at the  $x = k_p$  position for the bladder, of the  $p$  out of  $q$  movements. These shape structures start off as circles at  $t = 0$  and then evolve accordingly to emulate the human bladder collapse. The evolving shape descriptions (2.8), (2.9) are substituted in (2.7) to define the complete boundary condition.

Grids employed were in the range 50 by 50 to 200 by 200, and checks on their effects combined with the analytical comparisons below verified the high accuracy of the numerical solutions.

**2.2. Special-Case Analysis and Comparison**

Special-configuration analysis also provides some insight here. The computational work is checked through comparing with analytical results for a circle and a sphere, to find out if they agree with the numerical results. For a circle, sources and sinks of unknown strength  $m$  are deployed appropriately at the complex positions

$$z = 0, \quad z = i, \tag{2.10}$$

together with a uniform downward velocity

$$w(z) = imz, \tag{2.11}$$

in order to keep the urethral point fixed. The complex potential including images is thus found to be

$$w(z) = m(2 \ln(z + i) + iz). \quad (2.12)$$

In consequence, the stream function takes the form

$$\Psi(r, \theta) = 2m \tan^{-1}[r \sin \theta, 1 - r \cos \theta] + mr \sin \theta, \quad (2.13)$$

where we define  $-\pi/2 < \tan^{-1}(x) < \pi/2$ . The value of  $m$  is determined by matching to the normal squeeze velocity on the boundary. Similarly from use of Butler's theorem accompanied by sources and sinks, the analytical result for a sphere is

$$\begin{aligned} \Psi(R, z) = & aV \left( \sqrt{R^2 + z^2} + z \right) + a^2V \left( 1 + \frac{z + 1}{(R^2 + z^2 + 2z + 1)^{1/2}} \right) \\ & - aV \left( \sqrt{R^2 + z^2} + \frac{z + R^2 + z^2}{(R^2 + z^2 + 2z + 1)^{1/2}} \right) - \frac{V}{2} R^2, \end{aligned} \quad (2.14)$$

where  $V$  is the squeeze velocity and  $(R, z)$  are the axisymmetric coordinates of a sphere. The analytical results here are employed in comparisons later on.

### 2.3. End-Stage Analysis

Near the end of micturition the vessel usually becomes very thin. This is important in view of the velocities and pressures generated then. A model example is in Figure 4 for the case of a collapsing elliptical shape shown in horizontal or vertical formation, with semimajor and semiminor axis lengths  $a(t)$ ,  $b(t)$  in turn, while an analogous end-stage can be seen in Figure 3.

For a thin horizontal vessel, considering (2.6) and taking  $x \sim 1$  but  $y = h\bar{y}$  with  $\bar{y}$  of  $O(1)$  and the thickness parameter  $h$  small,

$$\Psi = \Psi_0(x, \bar{y}) + \dots, \quad (2.15)$$

we have to leading order simply

$$\Psi_{0\bar{y}\bar{y}} = 0, \quad (2.16)$$

in the majority of the vessel. This is for any thin vessel, including the thin horizontal ellipse say; we refer here to Figure 4 and refer forward to the small urethral-sphincter region which is also present. The asymptotic expansion treatment is given in detail in [15]. It follows from (2.16) that  $\Psi_0$  is at most linear in  $\bar{y}$  while the velocity component  $u$  is independent of  $\bar{y}$  and so the kinematic boundary condition holding at the upper and lower vessel walls  $f_1, f_2$  yields

$$-u_x \mathcal{F} = \mathcal{F}_t + u \mathcal{F}_x, \quad (2.17)$$

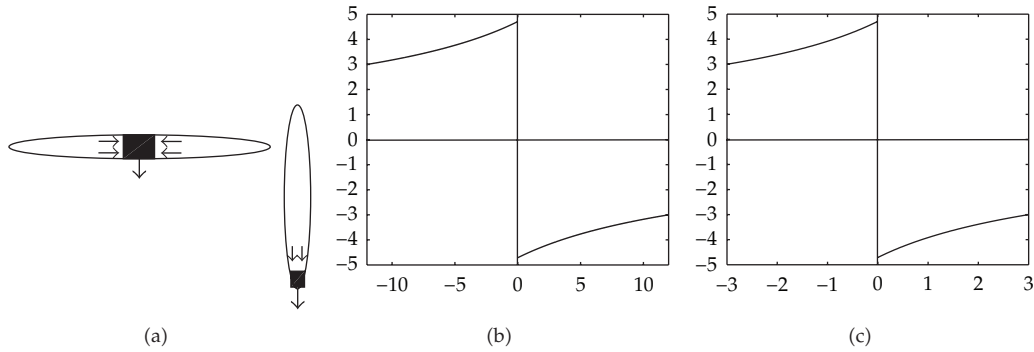


**Figure 4:** (a) Thin horizontal (left) and thin vertical (right) elliptical vessels. The sphincter region in black is shown. Incoming flows induced outside that region are also shown. (b, c) Plot of the velocity  $u$  (vertical axis) against  $x$  (horizontal axis) at time  $t = 0$  (b) for initial conditions  $a = 12$ ,  $b = 4$  (implies  $a' = -3$ ,  $b' = -1$ ), and at time  $t = 3$  (c). They look similar but on different scales.

where  $\mathcal{F} = f_1 - f_2$  is the scaled width of the vessel,  $u = U(x, t)$  is unknown, whereas  $\mathcal{F}$  is prescribed by the bladder movement. It is assumed in the results below that the vessel contracts inwards with its sides collapsing at the same rate as the top but the bottom remaining fixed. The slender-flow result (2.17) acts here to determine the induced velocity  $u$  and hence on integration the stream function and the internal pressure. As Figures 4(b) and 4(c) indicate, the squeezing process induces velocity components  $u$  which are nonzero, of opposite sign and directed towards each other at the mid-way station on the present scale. This leftover effect actually has other application in terms of fluid guns, but, in the present setting, it brings into play the smoothing-out phenomenon associated with a small part of the vessel close to the sphincter.

The smaller part of the vessel that is shown in Figure 4(a) on the left and is shaded in black is the sphincter region of size  $O(h)$  by  $O(h)$  in which the full Euler equations still hold at leading order when  $h$  is small, leading to the entire equation (2.6) in our setting of zero vorticity. This localised region occurs in the middle of the thin horizontal ellipse on the left and at the bottom end of the thin vertical ellipse on the right in Figure 4(a), for example, thereby surrounding the urethral sphincter position at the origin. Here,

$$\Psi = \bar{\Psi}(\bar{x}, \bar{y}) + \dots, \quad (x, y) = h(\bar{x}, \bar{y}), \tag{2.18}$$

so that  $\bar{x}$ ,  $\bar{y}$  are of  $O(1)$ . Substitution into (2.6) shows of course that  $\bar{\Psi}$  also satisfies (2.6) in full in terms of  $\bar{x}$ ,  $\bar{y}$ . As far as the boundary conditions are concerned, matching requires

$$\bar{\Psi}(\bar{x}, \bar{y}) \rightarrow \Psi_0(0\pm, \bar{y}) \quad \text{as } \bar{x} \rightarrow \pm\infty, \tag{2.19}$$

in view of the scalings, while  $\bar{\Psi}$  must remain constant along the walls  $\bar{y} = \bar{a} \sim 1$  for all  $\bar{x}$ ,  $\bar{y} = 0$  for  $\bar{x} < 0$  and  $\bar{y} = 0$  for  $\bar{x} > 0$ , taking different values there because of the sink embedded at the origin. The stream-function profiles on the right-hand side of (2.19) correspond to the left-over uniform velocity profiles produced via (2.17). The simplification

involved here is that the walls are effectively parallel to leading order. The matching in (2.19) thus accommodates exactly the incoming uniform streams that are induced by the longer-scale behaviour as indicated in Figures 4 and 5. (An analogous matching condition applies in the thin vertical case.) The localised solution can be written down explicitly as in the next paragraph. Moreover, there is general application here as anticipated at the start of Section 2 in the sense that this local flow structure surrounding the sphincter applies to viscous or inviscid flows with or without vorticity and to any vessel shape provided the vessel is thin.

Near the sphincter, the classical complex-variable result from [16] applies concerning in effect the flow into a channel through a narrow slit in the wall. However, in our case the flow is reversed as depicted in Figure 5(a). The channel has an  $O(1)$  breadth of  $\bar{b}$ . The fluid moves from the vessel out of it through the slit (sink) at  $O$ , which is placed at the origin in the  $z$ -plane where  $z = \bar{x} + i\bar{y}$ . The far-upstream or far-downstream points  $A, B, C, D$  are mapped conformally onto the real axis of a  $\zeta$ -plane as indicated in Figure 5(a). The relation

$$\zeta = e^{\pi z/\alpha} \quad (2.20)$$

gives the mapping, with  $\alpha$  the width of the channel.

Here  $B, C$  are taken to be coincident. The map opens out the walls into the real axis of the  $\zeta$ -plane so that  $B, C$  become the origin  $\zeta = 0$ . We now have a sink at  $\zeta = 1$  at the point marked  $O$  and a source at  $\zeta = 0$  corresponding to  $B, C$ . Thus, we obtain a complex potential

$$\omega = m \log \sinh \frac{\pi z}{2b}. \quad (2.21)$$

Separating this into its real and imaginary parts, we find the scaled velocity potential  $\bar{\Phi}$  and the stream function  $\bar{\Psi}$ ,

$$\begin{aligned} \bar{\Phi} &= \frac{1}{2} m \log \left( \cosh \left( \frac{\pi \bar{x}}{2b} \right)^2 \sin \left( \frac{\pi \bar{y}}{2b} \right)^2 + \cos \left( \frac{\pi \bar{y}}{2b} \right)^2 \sinh \left( \frac{\pi \bar{x}}{2b} \right)^2 \right), \\ \bar{\Psi} &= m \arctan \left( \sin \left( \frac{\pi \bar{y}}{2b} \right) \cosh \left( \frac{\pi \bar{x}}{2b} \right), \sinh \left( \frac{\pi \bar{x}}{2b} \right) \cos \left( \frac{\pi \bar{y}}{2b} \right) \right). \end{aligned} \quad (2.22)$$

The result is shown below in Figures 6(a)–6(c). Analogous working holds for the axisymmetric configurations of concern.

### 3. Computational and Analytical Results

The main computational results are presented in Figures 7–9 which show, respectively, a contour plot and velocity profiles near the finish of micturition, corresponding plots and profiles earlier in the collapse, and results for the analogous axisymmetric configurations (where radius replaces  $x$  in effect). The flow velocities and lengths are given here relative to reference values of collapse or squeeze velocity and bladder dimensions in turn for a typical micturition time of 17 seconds. The different scales required for the velocity plots as time varies are intriguing.



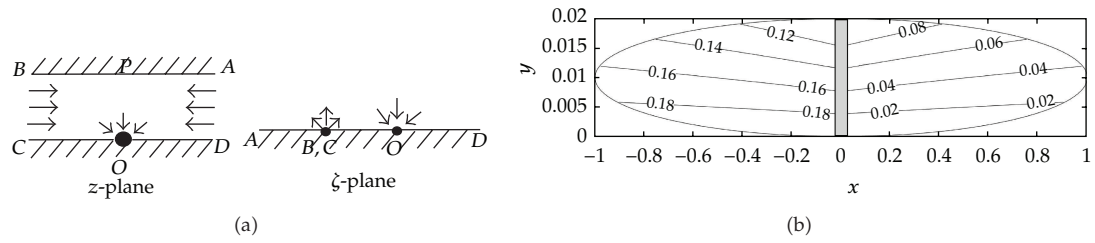


**Figure 5:** (a) Plot of the local flow problem in both the  $z$ -plane and the  $\zeta$ -plane. (b) Contours of the streamfunction  $\Psi \approx \Psi_0$  at time  $t = 0$  with initial conditions  $a = 1$ ,  $b = 1/100$ . The streamlines are all directed towards the centre  $x = 0$ . Concerning the shaded area in the middle, see Figure 6 for the solution closer to  $x = 0$ .

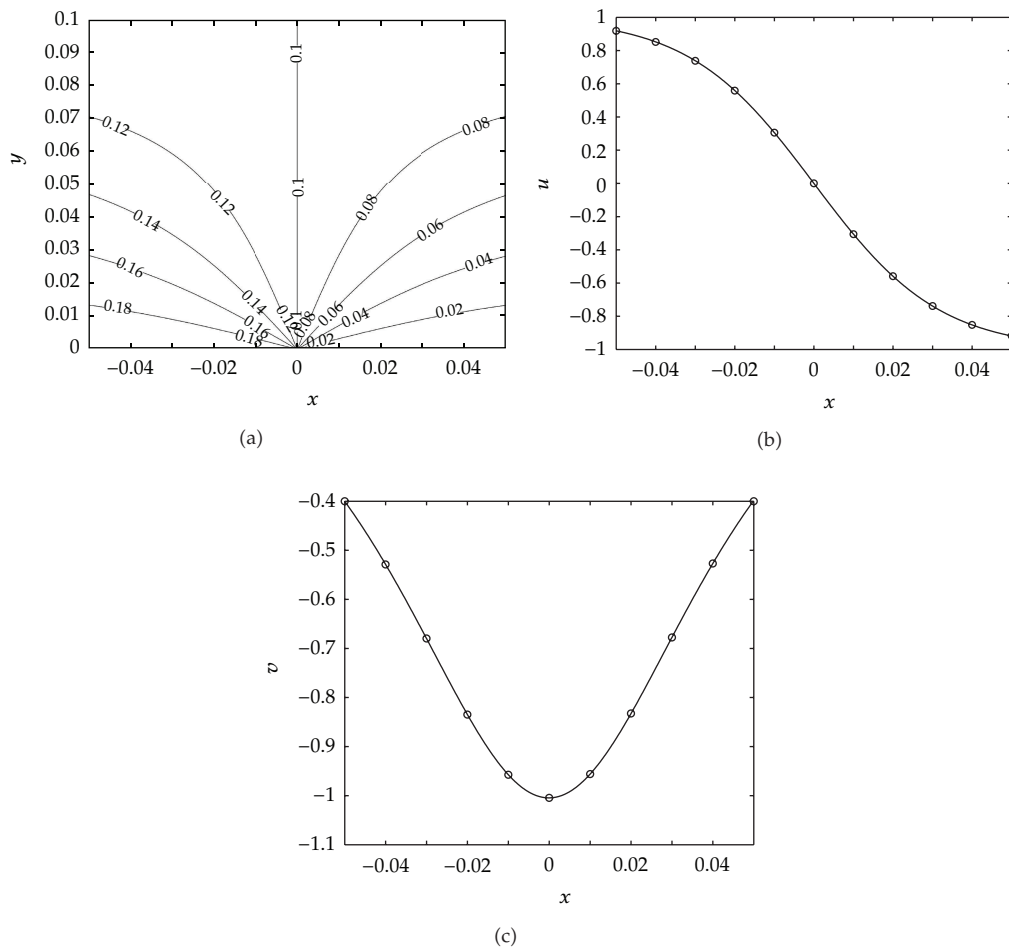


**Figure 6:** (a) Analytical streamlines of the two-dimensional flow for the horizontal Euler/Laplace local case shown in Figure 4(a). The streamlines are directed towards the origin. Also plotted are the (b) horizontal and (c) vertical velocities along the horizontal centreline for both the computational (small circles) and analytical (line) results.

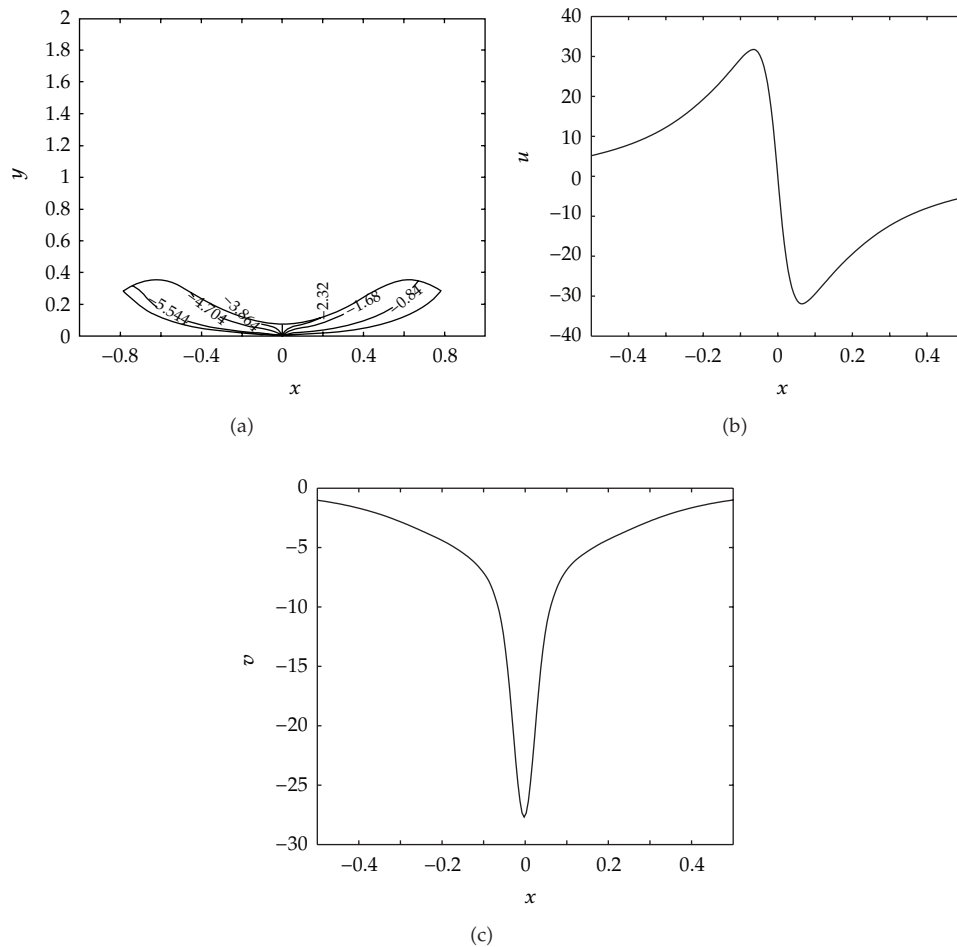


**Figure 7:** (a) Contour plot of the fluid motion within the modeled collapsing vessel (of Figure 3) near the end of micturition. Also plotted are the (b) horizontal and (c) vertical velocities along the horizontal centreline.

Before that, analytical checks such as in (2.13), (2.14), and Figures 4–6 all prove supportive: see also [15]. The agreement between the special-case analysis and the numerical work is found to be within half a percent error. On end-stage analysis, plotting (2.17) produces Figure 4 where it is noticeable that the induced horizontal velocity is directed towards the vessel centre, which is not surprising in view of the overall squeeze effect taking place. Moreover, the fluid speed increases towards the centre leaving a discontinuity there on the present length scales and this is then smoothed out locally as in Figure 6. A similar analysis holds for any vertical thin shape [15].

Comparing further the results of Figures 6 and 7 shows that the stream function and velocity are very similar indeed near the end of micturition. This is especially so in the vicinity of the sphincter in Figure 7(a), compared with the analytical result of Figure 6(a). The most visibly noticeable properties though from Figure 7 are the high velocities seen in (b) and (c). Large internal velocities and pressures are produced within the contained fluid near the end of micturition in a localised fashion as predicted by end-stage analysis. The same even applies during earlier stages in the collapse as in Figure 8. The velocities then are relatively

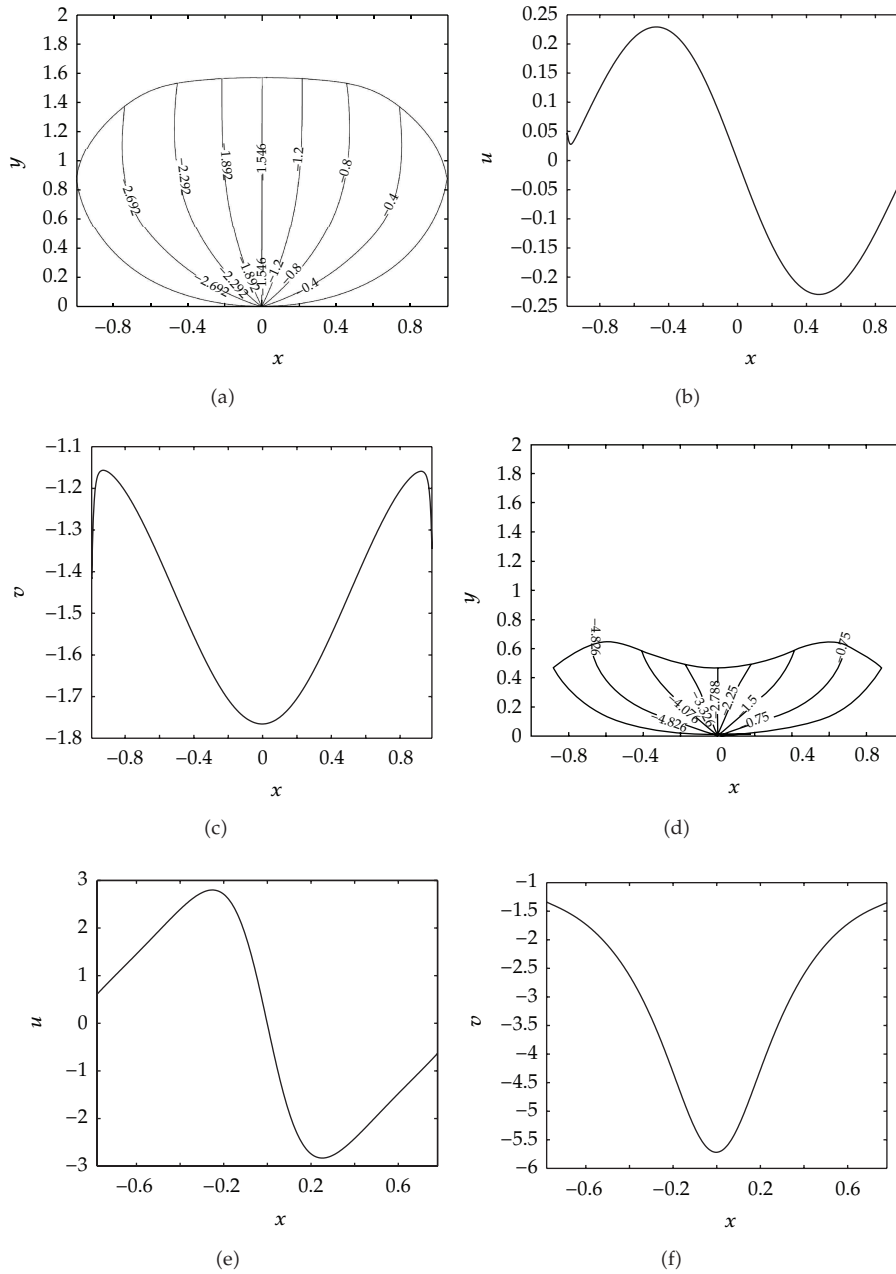


**Figure 8:** (a, d) Contour plots of the fluid motion within the modeled two-dimensional collapsing vessel (of Figure 3) during micturition, at mid-to-late times. Also plotted are the horizontal (b, e) and vertical (c, f) velocities along the horizontal centreline.

moderate but, as time passes and the vessel collapses further, velocities increase in line with the analysis.

The example of the collapse for an axisymmetric configuration shown in Figure 9 yields analogous findings. The results once again show, throughout, a significant increase in the induced flow velocities as the vessel collapses.

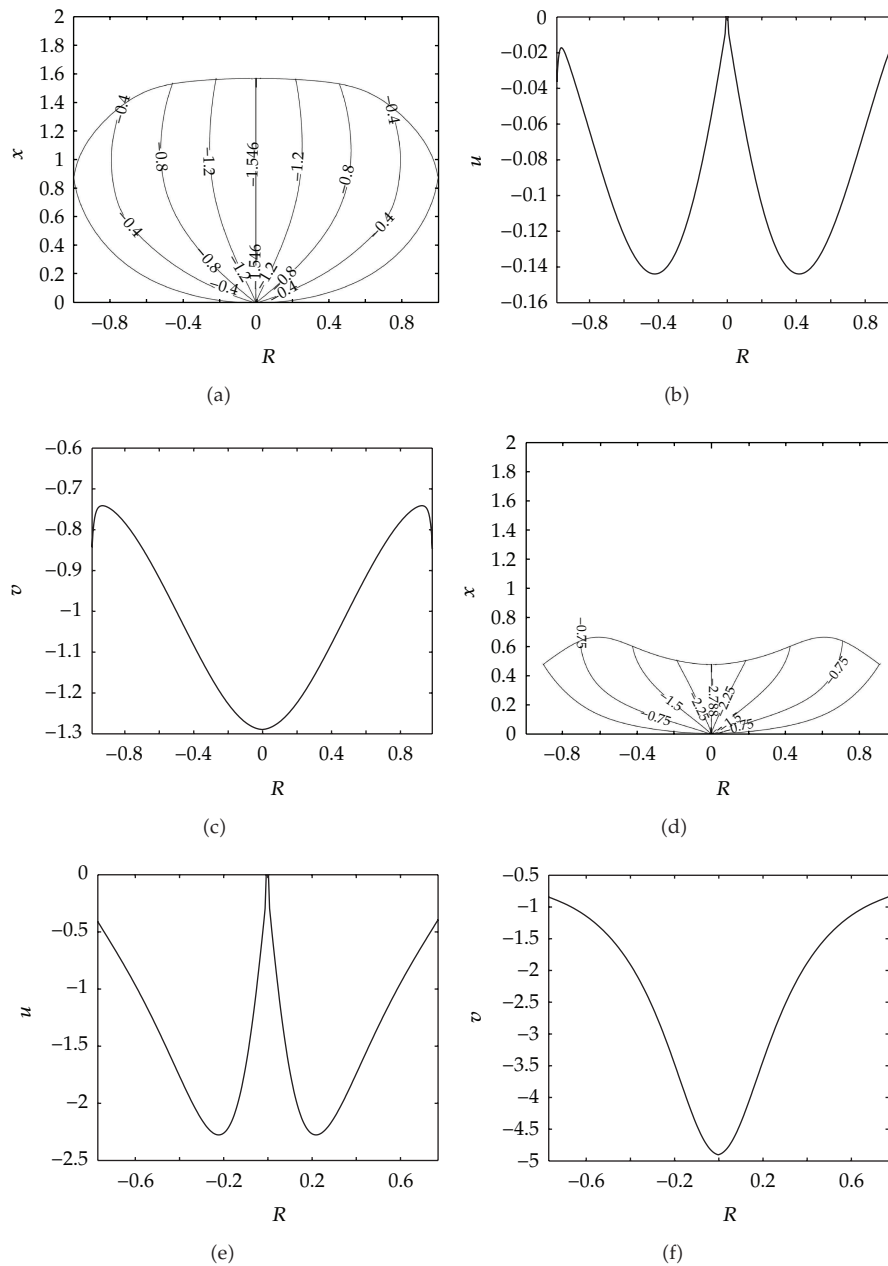


**Figure 9:** (a, d) Contour plot of the fluid motion within the modeled axisymmetric collapsing vessel during micturition. Also plotted are the horizontal (b, e) and vertical (c, f) velocities along the horizontal centreline.

#### 4. Final Comments

Two substantial findings of industrial and biomedical interest should perhaps be highlighted here. The first is the typical peak in the internal velocity profiles along with its large relative size and its continued growth and localisation throughout the micturition process. The second is the occurrence of areas of comparatively slow motion identified inside the

bladder vessel especially towards the vessel sides and, temporally, towards the end stage almost everywhere. These are sites where stagnation may occur and, bearing in mind the approximate 1-2 percent of bladder urine which remains not flushed out at each micturition, such sites are potentially unhealthy as regards overall flushing of the lower urinary tract.

Measurements of total flux from the urethra indicate that the collapse rate may vary with time in practice to mitigate both the growth of the peak and the slow-motion areas, but the peak appears inevitable anyway. Momentum in the downward direction (in addition to any inward) is converted into increasing horizontal urinary flow prior to almost vertical entry through the sphincter into the urethra. The peak would be there even in nonsymmetric configurations and in three dimensions. It is focused around the sphincter in every case, whether two-dimensional, axisymmetric, or fully three-dimensional. The maximal pressure produced internally is near the sphincter anyway because of the sink effect there; this becomes more so during the end stage as the instantaneous quadratic contributions from velocity to pressure dominate over the temporal-acceleration linear ones. The supplementary hydrostatic force which is normally around a 10–20 percent level in micturition is also overwhelmed during the end stage.

Notwithstanding the relative simplicity of the model, the combined analyses and computations here suggest we may usefully predict certain representative effects in quantitative terms. Thus, the relative horizontal velocities in Figures 7–9 correspond to maximal urinary speeds of 0.3–3 m/sec directed toward each other and pressure variations of the order of  $1000 \text{ kg/m}^3$ . It is also worth mentioning that, although the present results are in two-dimensional and axisymmetric configurations, they should lead the way for three-dimensional thinking of industrial interest and should give guidance for further research, including shape-flow interactions where necessary, even if such interactions are only secondary influences in the current context.

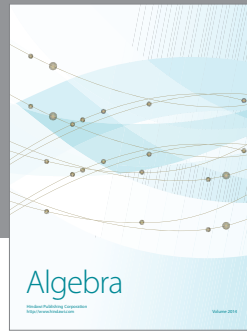
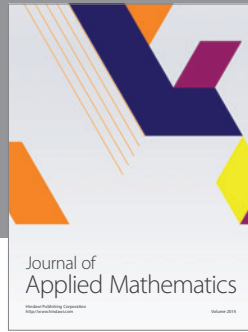
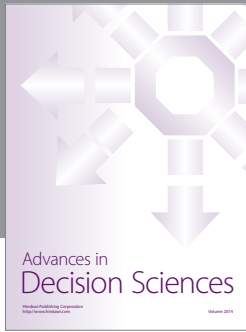
## Acknowledgments

Funding for this research came from Astellas Pharma Ltd and the Engineering and Physical Sciences Research Council (EPSRC) with a Cooperative Award in Science and Engineering (CASE). Many thanks also go to the UCL Medical Modelling Group and especially Professor Alan Cottenden for helpful discussions.

## References

- [1] P. Abrams, *Urodynamics*, Springer, 2006.
- [2] Radiology Malaysia, The official homepage of the College of Radiology, Academy of Medicine.
- [3] S. Croitoru, M. Gross, and E. Barneir, "Duplicated ectopic ureter with vaginal insertion: 3D CT urography with IV and percutaneous contrast administration," *American Journal of Roentgenology*, vol. 189, pp. w272–w274, 2007.
- [4] M. S. Damaser and S. L. Lehman, "The effect of urinary bladder shape on its mechanics during filling," *Journal of Biomechanics*, vol. 28-6, pp. 725–732, 1995.
- [5] D. J. Griffiths, *Urodynamics—The Mechanics and Hydrodynamics of the Lower Urinary Tract*, Hilger, 1980.
- [6] S. L. Waters, K. Heaton, and J. H. Siggers, "Ureteric stents: investigating flow and encrustation, Proceedings IMechE," *Journal of Engineering in Medicine H*, vol. 222, pp. 551–561, 2008.
- [7] R. I. Bowles, N. C. Ovenden, and F. T. Smith, "Multi-branching three-dimensional flow with substantial changes in vessel shapes," *Journal of Fluid Mechanics*, vol. 614, pp. 329–354, 2008.
- [8] *SEER Training Programs*, U.S. National Cancer Institute.
- [9] *Images and Scans*, Princeton University.

- [10] F. T. Smith, N. C. Ovenden, P. T. Franke, and D. J. Doorly, "What happens to pressure when a flow enters a side branch?" *Journal of Fluid Mechanics*, vol. 479, pp. 231–258, 2003.
- [11] F. T. Smith and R. G. A. Bowles, "Lifting multi-blade flows with interaction," *Journal of Fluid Mechanics*, vol. 415, pp. 203–226, 2000.
- [12] M. A. Jones and F. T. Smith, "Fluid motion for car undertrays in ground effect," *Journal of Engineering Mathematics*, vol. 45, no. 3-4, pp. 309–334, 2003, Practical asymptotics, I.
- [13] F. T. Smith and M. A. Jones, "AVM modelling by multi-branching tube flow: large flow rates and dual solutions," *Mathematical Medicine and Biology*, vol. 20, pp. 183–204, 2003.
- [14] F. T. Smith and A. S. Ellis, "On interaction between falling bodies and the surrounding fluid," *Mathematika*, vol. 56, no. 1, pp. 140–168, 2010.
- [15] M. Tziannaros, *Modelling bladder-collapse flow*, Ph.D. thesis, University College London, 2011.
- [16] L. M. Milne-Thomson, *Theoretical Hydrodynamics*, Courier Dover Publications, 1996.



# Hindawi

Submit your manuscripts at  
<http://www.hindawi.com>

